Biogeosciences Discuss., 9, 581–626, 2012
www.biogeosciences-discuss.net/9/581/2012/
doi:10.5194/bgd-9-581-2012

Biogeosciences Discussions

Estimation of the global inventory of methane hydrates in marine sediments using transfer functions

E. Piñero, M. Marquardt, C. Hensen, M. Haeckel, and K. Wallmann

Helmholtz Centre for Ocean Research Kiel, GEOMAR, Kiel, Germany

Received: 14 December 2011 – Accepted: 6 January 2012 – Published: 16 January 2012

Correspondence to: E. Piñero (epinero@geomar.de)

Published by Copernicus Publications on behalf of the European Geosciences Union.

Abstract

The accumulation of gas hydrates in marine sediments is essentially controlled by the accumulation of particulate organic carbon (POCar) which is microbially converted into methane, the thickness of the gas hydrate stability zone (GHSZ) where methane can be trapped, and the delivery of methane from deep-seated sediments by ascending pore fluids and gas into the GHSZ. Recently, Marquardt et al. (2010) developed a transfer function to predict the gas hydrate inventory in diffusion-controlled geological systems based on POCar and GHSZ. We present a new parameterization of this function and apply it to global datasets of bathymetry, heat flow, seafloor temperature and organic carbon accumulation estimating a global mass of only 91 Gt of carbon (GtC) stored in marine methane hydrates. Seepage of methane-rich fluids is known to have a pronounced effect on gas hydrate accumulation. Therefore, we carried out a set of systematic model runs with the transport-reaction code in order to derive an extended transfer function explicitly considering upward fluid advection. Using averaged fluid velocities for active and passive margins, which were derived from mass balance considerations, this extended transfer function predicts the formation of gas hydrates along the continental margins worldwide. Different scenarios were investigated resulting in a global mass of sub-seafloor gas hydrates of 400–1100 GtC. Overall, our systematic approach allows to clearly and quantitatively distinguish between the effect of biogenic methane generation from POC and fluid advection on the accumulation of gas hydrate and hence, provides a simple prognostic tool for the estimation of large-scale and global gas hydrate inventories in marine sediments.

1 Introduction

Submarine gas hydrates (GH) have been recovered in more than 40 regions worldwide and their presence has been deduced from geophysical, geochemical and geological evidences at more than 100 continental margin sites (e.g. Mazurenko and Soloviev,

BGD
9, 581–626, 2012

2003; Milkov and Sassen, 2002; Lorenson and Kvenvolden, 2007). They have been recognized as a key factor with respect to past and future climate change (e.g. Hester and Brewer, 2009; Adam, 2002; Archer, 2007; Lunt et al., 2011; Biastoch et al., 2011) and are considered as a new unconventional resource of natural gas (e.g. Sloan, 2003; Boswell, 2009). Models and observations clearly show that GH formation is essentially controlled by (1) the rate of accumulation of particulate organic carbon at the seafloor (POCar), (2) the kinetics of microbial degradation of organic matter and its related generation of methane, (3) the thickness of the gas hydrate stability zone (GHSZ), (4) the solubility of methane in pore fluids within the GHSZ, and (5) the ascent of methane-rich pore fluids and gas from deeper sediment strata into the GHSZ.

In contrast to the general progress in gas hydrate research made so far, the global abundance of GH in marine sediments still remains poorly constrained. Estimates are generally based on extrapolation of field data (e.g. Kvenvolden and Claypool, 1988; Dickens, 2001; Milkov, 2004) and geochemical transport-reaction modeling (e.g. Buffett and Archer, 2004; Klauda and Sandler, 2005; Archer et al., 2009; Burwicz et al., 2011). Although some of the earliest estimates were based on unrealistic conditions (e.g. Dobrynin et al., 1981) and can likely be excluded, they still range over three orders of magnitude (1×10^2–8×10^4 GtC; cf. Fig. 1) and a clearly constrained consensus value has not emerged over the past decades. This uncertainty implies a major draw-back since the resource potential and the possible impact of methane hydrates on past and future climate change cannot be evaluated without a well constrained estimate of global GH abundance and its distribution.

The availability of global data sets and the performance of global models greatly improved during the past decade. Grid-based transport-reaction modeling is thus a promising tool for the evaluation of global gas hydrate occurrences. Total estimates of GH based on globally gridded data were first published by Gornitz and Fung (1994) who used available information on bathymetry, ocean bottom temperature, organic carbon concentrations as well as averaged values of heat flow and thermal conductivity in marine sediments. The simplified assumption of a GH saturation of 5–10 vol % of pore

BGD
9, 581–626, 2012

space lead them to predict a global inventory of marine gas hydrates ranging from 14 200 to 74 700 GtC. Klauda and Sandler (2005) deduced the same range of GH saturations from systematic model runs with a modified version of the transport-reaction code of Davie and Buffett (2001) and predicted a mass of 64 500 GtC. However, Klauda and Sandler's estimate is unrealistic, because they assumed the entire POC pool to be degradable at a constant reactivity ($1.5 \times 10^{-14}\,s^{-1}$) – this is in contradiction to the general knowledge of organic matter degradation slowing down with time/age (e.g. Middelburg, 1989; Westrich and Berner 1984; Wang and Van Cappellen, 1996; Wallmann et al., 2006). Moreover, important microbial processes such as the degradation of organic matter via sulfate reduction and anaerobic methane oxidation (AOM) are not considered in their model. The studies of Buffet and Archer (2004) and, more recently, Archer et al. (2009) consider sulfate reduction and AOM as defined in the original model of Davie and Buffett (2001). For their best fit they assumed that 25 % of the total organic carbon is available for degradation, as well as distinct fluid flow velocities at passive and active margins, which were defined as a function of the sedimentation rate and compensated by downward fluid flow over 50 % of the global seafloor area. The total GH inventory of 3000 GtC (Buffet and Archer, 2004) was however affected by an extrapolation error and subsequently corrected downward to about 1000 GtC (Archer et al., 2009). Recently, Burwicz et al. (2011) presented a new global estimate based on 1-D model runs using the POC kinetic rate law proposed by Wallmann et al. (2006) for the formation of biogenic methane. Their budget ranges from 4 to 995 GtC and covers POCar values from the Holocene to enhanced accumulations during glacial times, but does not explicitly consider the effect of fluid or gas ascent.

The goal of the present study is to provide a systematic analysis that clearly distinguishes between the effects of POCar and fluid advection and to offer a simple, but realistic tool for the prediction of GH inventories. In a first step we apply a new parameterization of the transfer function presented by Marquardt et al. (2010), which considers GH formation from biogenic methane in diffusion-controlled systems, on gridded global datasets of the control parameters. Subsequently, an extended transfer function

BGD
9, 581–626, 2012

is developed, considering upward fluid advection and consequently providing a more realistic global budget of gas hydrates.

2 Data sources and methods

A transfer function for the quantification of methane hydrates in marine sediments was recently developed by Marquardt et al. (2010) based on the diagenetic transport-reaction model formulated by Wallmann et al. (2006). The study by Marquardt et al. (2010) revealed that the accumulation rate of particulate organic carbon (POCar) and the thickness of the GHSZ are the most important and independent parameters controlling the formation of GH from biogenic methane formed within the GHSZ. However, in order to derive their equation, Marquardt et al. consider a thickness of the GHSZ up to 2000 m, a value that is larger than the maximum thickness of the GHSZ in the global ocean (e.g. Wood and Yung, 2008). In order to correct possible biased results of the equation for narrow GHSZ and low POC inputs, we have done a number of extra model-runs of the same model presented in Marquardt et al. (2010), considering thicknesses of the GHSZ ranging from 228 to 610 m. Integrating all the results (122 simulations in total), and discarding the results of GHSZ thicker than 1000 m, we have performed a new multi-parametric fitting of the equation, applying the method of least squares to calculate the coefficients:

$$\mathrm{GHI} = a_1 \cdot L_{\mathrm{GHSZ}}^{a_2} \cdot \exp\left[-(a_3 - a_4 \cdot \ln[\mathrm{POCar}])^2\right] \quad (1)$$

with $a_1 = 0.0004 \pm 0.0001$; $a_2 = 1.73 \pm 0.03$; $a_3 = 1.78 \pm 0.03$; $a_4 = 0.64 \pm 0.01$ and where GHI is the integrated gas hydrate inventory in $\mathrm{gCH_4\,cm^{-2}}$ of seafloor area, POCar is the accumulation rate of particulate organic carbon in $\mathrm{g\,m^{-2}\,yr^{-1}}$ and L_{GHSZ} is the thickness of the GHSZ in m.

In general, this new fit produces more realistic results for low POCar and narrow GHSZ, with a variance of residuals of $20.4\,\mathrm{gCH_4\,cm^{-2}}$, and a linear correlation of the

BGD
9, 581–626, 2012

fitted curve (σ^2) of 0.9899. The linear correlation matrix of fit parameters can be found in Table A1.

The approaches and global datasets used to describe the two main parameters controlling gas hydrate formation are described in the forthcoming section. The transfer function was applied at each grid-point of the ocean in a spatial resolution of $1^\circ \times 1^\circ$. The total methane inventory was integrated by calculating the surface area for each cell of the grid, using the 1984 World Geodetic System ellipsoid as approximation of the shape of the Earth. Values below 0.1 $gCH_4\,cm^{-2}$ are in the expected error range, and therefore were discarded for the global calculations.

2.1 Accumulation rate of particulate organic carbon

The POCar depends on the total organic carbon flux to the seafloor (rain rate), the remineralization processes within the top of the sediment column, and the sedimentation rate, which generally decreases with increasing distance from the coastline and increasing water depth (e.g. Suess, 1980; Martens et al., 1992; Seiter et al., 2005; Romankevich et al., 2009; Zonneveld et al., 2010; Burwicz et al., 2011). Although POCar is simple to determine, the lack of global datasets on sedimentation rates is the main limitation in this regard. Moreover, model simulations show that time scales of some Ma are required to run a typical gas hydrate system into steady-state so that it is also important to consider the long-term sedimentary history. In order to find good approximations to the distribution of POCar in the world ocean, the following four options were considered. Scenarios 1 and 2 are approaches to derive data grids for recent sedimentation rates, while scenarios 3 and 4 aim to consider the sedimentation history by using crustal ages as time constraint.

BGD
9, 581–626, 2012

Approach #1

For Approach #1 we apply the new parameterization by Burwicz et al. (2011) where Holocene sedimentation rates are calculated as a function of water depth:

$$w = \frac{w_1}{1+\left(\frac{z}{z_1}\right)^{y_1}} + \frac{w_2}{1+\left(\frac{z}{z_2}\right)^{y_2}} \quad (2)$$

where w is the burial velocity in cm yr^{-1}, z is the water depth in m. The best fit to the measured data was obtained for $w_1 = 0.117$; $w_2 = 0.006$; $z_1 = 200$; $z_2 = 4000$; $y_1 = 3$ and $y_2 = 10$.

The distribution of burial velocities was calculated by applying Eq. (1) to a $1^\circ \times 1^\circ$ global dataset of bathymetry. Subsequently, the grid was combined with the global dataset of particulate organic carbon (POC) in surface sediments published by Seiter et al. (2004) to calculate the global distribution of POCar. In order to have a complete spatial coverage, the average of all POC data (0.58 wt. %) was used for data gaps in the Southern Ocean and the Southwestern Pacific. POCar was calculated with the following equation

$$\mathrm{POCar} = 100 \cdot \mathrm{POC} \cdot w \cdot d_S \cdot (1-\phi), \quad (3)$$

with POCar in gC m^{-2} yr^{-1} and POC in wt. %; w is the burial velocity in cm yr^{-1}; d_S is the density of dry sediment, i.e. 2.5 g cm^{-3}, and ϕ is the porosity. A porosity value of 0.8 for surface sediments is used in this calculation.

Approach #2

Approach #2 uses the rain rate of POC (POCrr) to estimate POCar values in the sediment applying the empirical equation recently published by Floegel et al. (2011) where POCar in shelf and deep-sea sediments are calculated as:

$$\mathrm{POCar}_{\mathrm{m\,arg\,ins}} = 0.2277\,\mathrm{POCrr}^{1.11} \quad (4)$$

BGD
9, 581–626, 2012

and

$$POCar_{deep-sea} = 0.01746 POCrr^{1.05}, \quad (5)$$

In the equation above POCar and POCrr are given as mass fluxes in $gC\,m^{-2}\,yr^{-1}$ whereas in the original equation by Floegel et al. (2011) the flux has units of $mmol\,m^{-2}\,yr^{-1}$ of C.

Continental margins were defined as the area within 200 Nm (~370 km) off the coastline (Fig. 3; orange and light blue coloring). Due to the high input of riverine particles to the Arctic Ocean, Eq. (4) was also applied for the area north of 60° N. To obtain a suitable data set for POC we used remineralization rates of POC (POCremi) for water depth >1000 m provided by Seiter et al. (2005) that were derived from global estimates of in situ benthic oxygen uptake. Since POCrr, POCar and POCremi are related by Eq. (6):

$$POCar = POCrr - POCremi, \quad (6)$$

where POCremi is the remineralized POC in $g\,m^{-2}\,yr^{-1}$ of C,

POCar was calculated by solving Eqs. (4), (5) and (6) using an iteration code in Matlab®. In order to extend the coverage of the calculation, the POCar calculated with Approach 1 was used in the areas where no POCrr data were available (<1000 water depth, Southwestern Pacific Ocean).

Approach #3

Because Approaches 1 and 2 only provide estimates for modern POCar values, which may not hold true for the longer geological time scales on which GH are formed, we provide a comparative dataset where we calculated a long term averaged burial velocity by combining data of the total thickness of marine sediments (Divins, 2010) with the age of the oceanic crust (NOAA, 2010). In order to avoid inconsistencies in young

BGD
9, 581–626, 2012

ages, and to prevent infinite values in further calculations, ages younger than 1 Myr were discarded.

$$w = \frac{\text{sediment thickness}}{\text{age of oceanic crust}} \left[\frac{\text{cm}}{\text{yr}}\right] \quad (7)$$

The resulting map is shown in Fig. A1.

Since Approach #3 lacks information about the long-term accumulation of POC we used a recently published equation by Marquardt et al. (2010) that relates POC concentrations to burial velocity (Eq. 8) to calculate POCar (using Eq. (3) and an average porosity of 0.5):

$$\text{POC} = 3 - 28 \cdot \exp[-44.5 \cdot w]. \quad (8)$$

Approach #4

Approach #4 is a slight modification of Approach #3, where modern POCar was calculated as for Approach #1 using the POC dataset published by Seiter et al. (2004) and Eq. (3). Approaches #3 and #4 do not consider the deposition of sediments and POC in continental shelf and slope areas located on continental crust.

2.2 Thickness of the gas hydrate stability zone

The global thickness of the GHSZ was calculated applying the equation provided by Tishchenko et al. (2005) to global grids of bathymetry (Amante and Eakins, 2009), bottom water temperature, and geothermal gradient. A global grid of averaged bottom water temperatures over the last 20 yr using the Ocean General Circulation Model (OGCM) (Barnier et al., 2006) was kindly provided by A. Biastoch. Geothermal gradients were calculated based on heat flow models by Pollack (1993) and Hamza et al. (2008). In general, both distribution maps of the heat flow show a similar pattern. The absolute values of heat flow anomalies of Hamza et al. (2008) are generally lower,

BGD
9, 581–626, 2012

with values up to 150 mWm^{-2} compared to values up to 350 mWm^{-2} presented by Pollack et al. (1993). Regions of major discrepancies between both approaches are located along major mid-oceanic ridges (e.g. South East Indian Ocean; South Mid Atlantic Ridge), where GH are not forming anyhow because heat flow is typically too high and POCar very low.

Although the estimation of thermal conductivities has been a focus of major interest for the petroleum industry, there is still not a unique value or a unique way to calculate it. Among the number of means that can be used to calculate the weight of each component (minerals and fluids) in the total thermal conductivity of sediments, the geometric mean is the most accepted one (e.g. Clauser and Huenges, 1995).

$$\lambda = \lambda_{\text{min}}^{1-\phi} \cdot \lambda_{pw}^{\phi} \tag{9}$$

where λ is the thermal conductivity in Wm^{-1} K^{-1}, min is mineral, pw is pore water, and ϕ is porosity.

Considering a thermal conductivity of 0.9–3 Wm^{-1} K^{-1} for clays (Fjeldskaar et al., 2009), 0.6 Wm^{-1} K^{-1} for pore water in marine sediments (e.g. Deming and Chapman, 1989), and an average porosity of 0.5 over the sediment column, the thermal conductivity of sediments was estimated at 0.7–1.34 Wm^{-1} K^{-1}. For simplicity, and following previous works, a value of 1 Wm^{-1} K^{-1} was used in our calculations (e.g. Wood and Yung, 2008; Jung and Vogt, 2004). A density of 1000 kg m^{-3} for water was considered to estimate the hydrostatic pressure at each grid point. The thickness of the GHSZ was reduced to the total oceanic sediment thickness (Divins, 2010) where this value was exceeded.

BGD
9, 581–626, 2012

3 Results and discussion

3.1 Accumulation of organic carbon

In general, POC-rich sediments accumulate in areas of high marine productivity. POC remineralization and preservation strongly depends on environmental conditions such as sedimentation rate, terrigeneous input, bottom water oxygenation, etc (e.g. Cai and Reimers, 1995; Hartnett et al., 1998; Hartnett and Devol, 2003; Seiter et al., 2005).

The four approaches presented here to calculate POCar resulted in different distribution patterns and show a total range of about one order of magnitude for global POCar (Fig. 4). Absolute values range from 1×10^{-4} – ~25 gC m^{-2} yr^{-1} in the abyssal plains of the Pacific and rapidly accumulating continental margins, respectively. However, the highest values (>10 gC m^{-2} yr^{-1}) are restricted to the shallow shelf of the Circum-Arctic realm and other areas, where marine GH are not stable. The highest global POCar of 1.54×10^{14} gC m^{-2} yr^{-1} was obtained from Approach #2 (Table 1). Interestingly the distribution pattern is similar to the previously published map of POC accumulation rates in marine sediments by Romankevich et al. (2009) although a quantitative comparison is not possible because Romankevich's data are not available in a digital format.

Approach #2 is based on POC degradation rates in marine surface sediments calculated from in-situ oxygen flux measurements at the sediment-water interface (Fig. 3). The general distribution pattern along the margins is in agreement with comparable data sets (e.g. POC distribution, Seiter et al., 2004), but the overall range of values is reduced and typically varies by less than one order of magnitude. A major hotspot is predicted for the continental margin of Oman and Pakistan (26 gC m^{-2} yr^{-1}), and elevated values for the western continental margins of Africa and America, which is in accordance to known GH occurrences.

The new estimates of Holocene POC accumulation obtained by Approach #1 and Approach #2 ($1.44–1.54 \times 10^{14}$ gC yr^{-1}; see Table 1) are very close to each other even though they are based on independent data sets. They also agree with a previous estimate derived from POC concentration data and Holocene sedimentation rates

BGD
9, 581–626, 2012

collected by Russian scientists (1.40×10^{14} gC yr^{-1}; Baturin, 1997). These conformities strongly support the validity of Approach #1 and Approach #2.

The approaches based on the averaged sedimentation rate over time (#3 and #4) show very similar distributions. However, both approaches suffer from a lack of data for large continental margin areas such as the Arctic Ocean, the Mediterranean Sea and other marginal seas, where age data are not available. These areas coincide with some of the main deposition areas during the Holocene (and likely during the late Neogene), resulting in much lower POCar values as compared for those of the Holocene scenarios (#1 and #2; Table 1). Due to these restrictions Approaches #3 and #4 are clearly not the preferred scenarios, but can serve as lower boundary estimates for POCar.

3.2 Thickness of the gas hydrate stability zone

Gridded data of the geothermal gradient used in this study are based on the spherical harmonic approximations of heat flow by Pollack et al. (1993) and Hamza et al. (2008). The spherical harmonic approach does not always fit to measured data, especially in a number of places where crustal flow highly affects the temperature distribution in the sediments (e.g. Costa Rica margin; Grevemeyer et al., 2004). However, both approaches reveal very similar results in terms of GHSZ thickness for most parts of the global ocean. They are also in agreement with recently published data by Wood and Yung (2008). The greatest thickness of the GHSZ is found at continental margins with thick sediment covers and where low bottom water temperatures and low geothermal gradients prevail (such as circumpolar regions and passive margins in the Atlantic and Indian Ocean; Fig. 5). In general, both approaches are also in good agreement with recent reports on BSR depth (e.g. 240 mbsf on the Northern Cascadia margin; Riedel et al., 2006; 200 mbsf on the Svalbard margin; Hustoft et al., 2009; 500 mbsf on the Blake Ridge; Holbrook et al., 1996; 450 mbsf; Pecher et al., 1998). However, the comparison of BSR depths at various ODP sites (Marquardt et al., 2010) generally revealed a better match to Hamza's approach that will therefore be treated as the preferred case study.

BGD
9, 581–626, 2012

A major uncertainty in our approach is the value of the thermal conductivity of marine sediments. A value of $1\,W\,m^{-1}K^{-1}$ seems to be a well accepted value (e.g. Woods and Jung, 2008, Reitz et al., 2007), and is in good agreement with direct thermal measurements on surface and shallow marine sediments in a number of continental-margin sites (e.g. Kaul et al., 2006). However, thermal conductivity can be expected to increase with depth due to porosity reduction, compaction and cementation. For comparison, a thickness of the GHSZ of up to 900 m is calculated applying a thermal conductivity of $1.5\,W\,m^{-1}K^{-1}$, which can be considered as expected value at several hundred meters deep in the sedimentary column. The distribution maps of the thickness of the GHSZ in this case (not included here) are in good agreement with previous published results by Burwicz et al. (2011).

3.3 Global gas hydrate inventory I

In general, resulting estimates of the global gas hydrate inventory for approaches #1–#4 and different heat flow models (see Sects. 3.1 and 3.2) are very low (1 to 91 GtC; Table 1) compared to most previous estimates (cf. Fig. 1). The results are only similar to that of Burwicz et al. (2011) which was based on the same kinetic approach, and similar gridded data sets as Approach#1 for POCar. Differences with their result are attributed to offsets between the numerical model and the transfer function (Marquardt et al., 2010). However, the generally close match between both results (1 GtC to 4 GtC) confirms the validity of the transfer functions as useful and simple tools to calculate GH inventories.

As expected, the choice of the heat flow grid (Hamza's or Pollack's) does not have a major effect on the result, and hence the 2 orders of magnitude difference is clearly caused by the high range of POCar predictions presented above. Perhaps counter intuitively, Approach #1 and Approach #2 with similar global POCar accumulations yield considerably different GH estimates. However, as outlined above Approach#1 predicts a very high proportion of POC to occur on shallow shelf areas where GH is not stable. Clearly speaking, for this scenario there is an obvious mismatch between areas with

BGD
9, 581–626, 2012

high methane-formation potential (high POCar) and those providing the best conditions for GH stability. On the other hand, this behavior is not so extreme in Approach #2.

Figure 6a shows the resulting distribution map of GH using Approach #2 for POCar and Hamza's heat flow. The function only predicts the occurrence of significant amounts of GH at continental margins with high POCar (e.g. Oman-Pakistan, Angola-Namibia, Peru, Arctic Ocean), including both passive and active margins. In most of these regions GH have been previously recovered or inferred by geophysical detection of a BSR (e.g. Lorenson and Kvenvolden, 2007).

Equation (1) restricts the occurrence of significant amounts of GH ($1.5\,gCH_4\,cm^{-2}$) to a threshold value for the thickness of the GHSZ of ~200 m and a POCar of $\sim 2\,gC\,m^{-2}\,yr^{-1}$ (Fig. 6b). However, considerable amounts of gas hydrate ($4\,gCH_4\,cm^{-2}$) are only formed at POCar $>5\,gC\,m^{-2}\,yr^{-1}$ (Fig. 6a). These values define both the minimum residence time of POC within as well as the minimum POC flux into the GHSZ required for the generation of sufficient amounts of methane to form GH. The POCar threshold value of $5\,gC\,m^{-2}\,yr^{-1}$ corresponds to an average sedimentation rate of $30\,cm\,kyr^{-1}$ and POC content of 0.4–0.5 wt. %, which has been previously identified as the minimum POC content required for GH formation (e.g. Collett, 1995; Mac Donald, 1990; Klauda and Sandler, 2005). Most of the values calculated for GHSZ thickness and POCar over the world oceans are below these thresholds (white dots in Fig. 6b), which is ultimately the reason for obtaining only a few isolated patches of significant GH concentrations in Fig. 6a. Obviously, this result corresponds in no way to observations in natural systems (cf. compilations by Kvenvolden and Lorenson, 2001 or Maslin et al., 2010). The major reason for this mismatch is that the model approach oversimplifies the conditions in complex geological systems, at least with respect to transport processes. The numerical model, which formed the basis for the transfer function developed by Marquardt et al. (2010) only considered sedimentation, diffusion, and compaction-driven pore water advection (not producing a net upward flow). However, major GH accumulations are related to enhanced fluid and gas advection (e.g. Torres et al., 2004; Buffett and Archer, 2004; Milkov, 2005), which clearly shows

BGD
9, 581–626, 2012

the need for an improved transfer function in order to produce more realistic estimates of GH inventories.

3.4 Derivation of an extended transfer function considering fluid flow

In order to systematically analyze the effect of upward directed fluid flow on gas hydrate formation, we performed a new series of model runs with the original numerical model (Wallmann et al., 2006; Marquardt et al., 2010). The model explicitly considers steady state compaction of the sediment, diffusive and advective transport of dissolved constituents, input and degradation of POC and particulate organic nitrogen (PON) via sulfate reduction and methanogenesis, anaerobic oxidation of methane (AOM), as well as the formation (and adsorption) of NH_4, dissolved inorganic carbon (DIC) and methane (CH_4). The model calculates the solubility of methane in pore water with respect to the stability field of gas hydrates and considers the formation and dissociation of GH, as well as the formation and dissolution of free methane gas in pore water. When methane concentration exceeds the solubility conditions for gas hydrates or free gas, gas hydrates precipitate or free methane gas accumulates in the pore volume. Gas hydrates dissociate when they are buried below the three phase equilibrium curve described by Tishchenko et al. (2005). The upward transport of gas by rising bubbles is not considered in the model. The POC-degradation rate is calculated as a function of POC input considering the decrease of the reactivity of POC with depth, as a combined effect of POC ageing and the inhibition effect of the accumulation of the degradation products (e.g. DIC and CH_4) in pore water (Wallmann et al., 2006). Input parameters and boundary conditions for the standard model are shown in Table 2. For an extensive description of the model, the reader is referred to the original publications by Wallmann et al. (2006) and Marquardt et al. (2010).

Model-runs were performed systematically imposing upward fluid flow velocities of 0.05, 0.1, 0.2, 0.3, 0.5, 0.75, 1, 1.5 and 2 mm yr^{-1}, and covering a wide range of variations of POCar and GHSZ typically found in continental margin environments (GHSZ of 228–1745 m; POCar of 0.7–37.4 gC m^{-2} yr^{-1}). In total 460 model runs were performed.

BGD
9, 581–626, 2012

For all model runs the concentrations at the upper boundary of the dissolved species SO_4, CH_4 and NH_4 were fixed accordingly to values of the standard seawater composition (Dirichlet conditions). For each model-run, the concentrations of CH_4, DIC and NH_4 in the advecting fluid (lower boundary) were derived from the concentrations at the lower boundary in model-runs neglecting fluid advection (Dirichlet conditions). Exemplarily, a series of model results for fluid flow velocities (FF) ranging from 0 to 1 mm yr^{-1} and constant POCar and thickness of the GHSZ (4.3 gC m^{-2} yr^{-1} and 376 m, respectively) is shown in Fig. 7. Dissolved methane concentrations increase in response to fluid flow while the sulfate penetration depth and the zone of intense AOM are shifted towards the sea floor with increasing fluid velocity. On the other hand, the increase of reaction products in pore water (DIC, CH_4) causes a slight decrease of POC degradation with increasing fluid advection. However, due to the methane transported from below the GHSZ, the total rates of GH formation increase with increasing fluid flow.

The result of the systematic analysis of the three key parameters, the thickness of the GHSZ, POCar and fluid advection is shown as dots in Fig. 8. For constant POCar (4.35 gC m^{-2} yr^{-1}), GH formation increases with both fluid flow and the thickness of the GHSZ (Fig. 8a). For a constant fluid flow of 0.2 mm yr^{-1} and variable thickness of the GHSZ, GH concentrations generally decrease with increasing POCar (Fig. 8b). At low POCar values, FF is more effective, generating more GH. As higher POCar are associated with higher sedimentation rates (SR) and outweigh the positive effect of fluid advection, GH accumulation decreases until a minimum is reached at 7.4 gC m^{-2} yr^{-1}, where FF = SR. In this range of values, FF is lower than the SR, and therefore, it is no more effective. Beyond the critical point, GH accumulation increases with the POCar, due to the enhanced POC concentration until a relative maximum is reached at ~10 gC m^{-2} yr^{-1}. After this maximum, the system is controlled by the chemical products of organic matter degradation (DIC and CH_4), and GH concentrations slightly decrease again. Hence, the thickness of the GHSZ has generally a positive effect on GH formation, while the relation of POCar and fluid advection in the model shows a more complex behavior. The latter aspect is further evaluated in Fig. 8c, which shows the

BGD
9, 581–626, 2012

results of a series of model runs considering a constant thickness of the GHSZ (376 m) and a range of POCar values (from 2.21 to 17.93 $gC\,m^{-2}\,yr^{-1}$) as a function of fluid velocities ranging from 0 to 0.6 $mm\,yr^{-1}$. The complex behavior of the GH concentration curves can be best explained (and generalized) looking at the green data points in Figure 8c (POCar of 17.9 $gC\,m^{-2}\,yr^{-1}$). For fluid flow values (FF) generally lower than SR, the increase of FF causes a slight increase and then a decrease of GH masses towards a critical point, where FF = SR. The parabolic behavior of the curves for FF<SR may be explained as follows: Because there is no net upward advection of pore water, the general effect of FF is low. However, increasing FF extends the residence time of the pore water within the GHSZ and therefore more GH may form. Towards the critical point GH decreases again, because of the negative effect of CH_4 and DIC enrichment on POC degradation (cf. Wallmann et al., 2006). Beyond the critical point (FF>SR), the increase in gas hydrate concentration is distinctly enhanced, showing a nearly linear behavior. The slope of this line decreases with the POCar similarly to Fig. 8b and increases with the thickness of the GHSZ. The position of the critical point for each series of model runs is a function of the sedimentation rate (included in POCar) and relative to the given fluid flow.

The general decrease in GH with increasing POCar (Fig. 8b) is partly a result of the constant concentration of methane applied as lower boundary condition of the model-runs. The constant concentration implies that enough methane is generated below the GHSZ to support a constant methane-rich FF from below until the steady state is attained. However, in a real geological system, the methane supply may be in fact limited by the methane generation at depth, which is fueled by the POCar, which was also taken as constant. Thus, low POCar values actually may limit the methane supply from below and thereby the GH accumulation within the GHSZ. Therefore, the results of the model are only valid if POCar is constant for a considerable period of time (~1 Myr), and there is no shortage of methane generation below the GHSZ.

BGD
9, 581–626, 2012

The critical points that limit the two behavior domains for all model runs can be fitted by a simple function as:

$$FF = b_1 \cdot POCar, \tag{10}$$

where $b_1 = 0.027 \pm 0.001$.

The results of the parameter analysis could be fitted by 2 empirical functions indicated by lines in Fig. 8a, b and c. Since globally GHSZ thicker than 600 m are very rare (see Fig. 5), the model-runs for GHSZ thickness >1000 m were excluded of the fitting. Overall, 293 results were fitted in:

for $FF \leq b_1 \cdot POCar$,

$$GH_{FF} = GHI + b_2 L_{GHSZ}^{b_3} \cdot \exp\left[-b_4 \cdot POCar^{b_5} \cdot (FF - b_6 \cdot b_1 POCar)^2\right]; \tag{11a}$$

and for $FF \geq b_1 \cdot POCar$,

$$GH_{FF} = GHI + b_7 \cdot L_{GHSZ}^{2 \cdot b_3} \cdot \exp\left[-(b_8 + b_9 \cdot \ln POCar)^2\right] \cdot (FF - b_1 POCar). \tag{11b}$$

with $b_2 = 0.054 \pm 0.008$; $b_3 = 0.87 \pm 0.02$; $b_4 = 114763 \pm 85465$; $b_5 = -2.8 \pm 0.2$; $b_6 = 0.66 \pm 0.05$; $b_7 = 0.0044 \pm 0.0008$; $b_8 = 0.20 \pm 0.05$; and $b_9 = 0.36 \pm 0.01$. The coefficients of both equations were determined in a combined least-square fit to the results of the numerical model with distinct parameter settings shown above.

A major uncertainty for the equation yields in the combination of SR and POC concentrations into the single parameter POCar. Although the model uses POC and SR as independent input parameters, a general correlation between POC concentration and SR exists (e.g. Henrichs, 1992; Tromp et al., 1995; Burdige, 2007). Based on measured data all over the oceans, Marquardt et al., (2010) present an equation to express this relation, which was used to calculate POC in our model-runs as a function of SR (Eq. 8). However, in this equation exists a big uncertainty, which is derived from the wide dispersion of the fitted data of up to 2 orders of magnitude, specially affecting low POCar values (Fig. 10; in Marquardt et al., 2010).

BGD
9, 581–626, 2012

To further test the accuracy of the extended transfer functions (Eqs. 11a and b), we calculated the GH content using the same parameters as for the numerical model runs. The extended transfer function reproduces the modeled data very well. Most data points plot along the 1:1 correlation line (Fig. 9). The general scatter is low, with a correlation coefficient (σ^2) of 0.9857 and a variance of residuals of 19.7 $gCH_4\,cm^{-2}$. The linear correlation matrix of fit parameters can be found in Table A2. As mentioned above, deviations correspond to low values of POCar, as well as combinations of FF and POCar near the critical point (SR = FF). Because of the strong change in GH concentration gradients for low POCar values, slight discrepancies between the real curve and the fit function (Eq. 10) may produce strongly biased results. Overall, the significance of those outliers is sufficiently low (Fig. 9) so that the extended transfer function can be used as a reliable tool to approximate marine GH inventories.

3.5 Global gas hydrate inventory II

While global data sets for GHSZ and POCar are available (although subject to considerable uncertainties, cf. 3.1, 3.2) such information is not available for FF. In continental margins, the most important mechanisms generating fluid migration are the mechanical reduction of porosity (compaction, compression) and diagenetic and metamorphic processes (release of water from breakdown of hydrous minerals, gas production) (e.g. Kopf, 2002; Kastner, 1999). As mentioned above, normal compaction does not directly lead to a net upward fluid flow, and hence values for FF cannot be easily derived from empirical equations of porosity reduction. In fact, fluid velocities have only been calculated for a limited number of areas where focused fluid flow preferentially occurs (e.g. mud volcanoes, cold seeps, etc), ranging from few mm to several m yr^{-1} (e.g. Wallmann et al., 1997; Linke et al., 2005). However, because these fluid pathways are neither homogenously distributed nor representative for larger areas of the seafloor those values for FF cannot be extrapolated.

A rough but valid method is to approach the global upward FF at continental margins by mass-balance considerations based on a steady-state pore water budget

BGD
9, 581–626, 2012

(Wallmann et al., 2011). Due to compaction, porosity of sediments decreases with increasing sediment depth, which can be described by empirical relationships (e.g. Einsele, 2000). However, a significant volume of pore water remains within the sediment after steady-state compaction. The global rate of pore water burial after compaction (PW_f in $cm^3\,yr^{-1}$) may be estimated from the global sedimentation rate ($SR_{glob} \sim 20 \times 10^{15}\,g\,yr^{-1}$, derived from Eq. (2) using the bathymetric grid), the mean density of dry solids ($d_S = 2.5\,g\,cm^{-3}$) and the porosity after compaction ($\Phi_f = 0.2 - 0.3$):

$$PW_f = \frac{\phi_f \cdot SR_{glob}}{d_s \cdot (1 - \phi_f)} \quad (12)$$

The resulting value for PW_f is 2.0.–3.4 $km^{-3}\,yr^{-1}$. Independent estimates of upward fluid flow at active continental margins yield a range of 1–2 $km^{-3}\,yr^{-1}$, (Von Huene and Scholl, 1991; Moore and Vrolijk, 1992; Jarrard et al., 2003) indicating that a major part of the buried pore fluids is mobilized by tectonic over-pressuring. For simplicity, we assume that total FF at active margins ranges from 1 to 2 $km^3\,yr^{-1}$ and from 1 to 1.5 $km^3\,yr^{-1}$ at passive margins, with combinations of both ranging from 2 to 3.5 $km^3\,yr^{-1}$.

Taking into account the respective extension of active and passive margins (Fig. 3), and a porosity at the upper limit of our model of 0.75 (excluding the uppermost bioturbated sedimentary column, Marquardt et al., 2010), fluid velocities of 0.1027, 0.1533 and 0.2053 mm yr^{-1} were obtained at active margins for 1, 1.5 and 2 $km^{-3}\,yr^{-1}$, respectively. Fluid velocities of 0.02 and 0.03 mm yr^{-1} were obtained for total fluid expulsion of 1 and 1.5 $km^3\,yr^{-1}$ at passive margins. These values are in the same range as previously published averaged values (e.g. Buffett and Archer, 2004), and fluid flow values determined for diffusive systems in the Cascadia margin (0.17 mm yr^{-1}; Malinverno et al., 2008). Thus, the flux of dissolved methane into the GHSZ may be estimated in 1.7–11.5 $TgCH_4\,yr^{-1}$, assuming a concentration in the pore fluids of 55–205 $mmolCH_4\,l^{-1}$ (Table 2), and taking into account the porosity reduction due to burial.

BGD
9, 581–626, 2012

The resulting ranges of estimates of the inventory of GH with the extended transfer function (Eqs. 11a and b) are listed in Table 1. There are considerable differences in the predicted global mass of GH with respect to the chosen method of calculating POCar. Generally, Approaches #1 and 2 using Holocene sedimentation rates result in higher estimates (400–1100 GtC) than Approaches #3 and 4 (300–500 GtC) using long-term averages of sedimentation rates. Figure 10 shows the resulting GH distribution map using the preferred combination of approximate POCar and GHSZ (Approach #2 and Hamza's heat flow model), and fluid flow velocities of 0.02 and 0.1533 mm yr^{-1} at passive and active margins, respectively. The map shows that minimum concentrations of 2–3 $gCH_4\,cm^{-2}$ stored in GH are typical for almost all the margin areas. Maximum concentrations of up to 21 $gCH_4\,cm^{-2}$ are predicted for the active continental margins off Chile and Alaska, as well as Japan, Taiwan and Indonesia, which are characterized by high POCar and thick GHSZ. A detailed example of the effect of the fluid flow distribution in active and passive margins, specific for Approach#2 for POCar and Hamza's equation for heat flow, is shown in Table 3. Enhanced fluid flow at active margins has a major effect on the total GH budget, while fluid flow at passive margins is anyway so low that it only produces minor effects on the global scale. Moreover, FF at active margins shows an effect of a factor of 1.5 in the global estimation of GH. As already discussed in Sect. 3.1, the use of long-term averages of sedimentation rates (Approaches #3 and 4) can only be regarded as minimum estimates, because large areas underlain by continental crust are neglected. Hence, due to the considerations above, our best estimate for the global sea floor inventory of GH is 400–1100 GtC.

Although our estimate is in the range of some previous estimates, and hence may be simply regarded as another method to come to the same result, we believe that this approach implies some clear improvements to previous studies: (1) the systematic analysis reveals a clear distinction of the control parameters of GH formation. (2) We used improved, state-of-the-art gridded data sets for the global calculation of control parameters. (3) In contrast to some previous studies (e.g. Buffett and Archer, 2004; Klauda and Sandler, 2005) we used a calibrated kinetic model of subsurface methane

BGD
9, 581–626, 2012

generation and a valid mass balance approach for calculating FF at continental margins. (4) We provide a simple and realistic tool to calculate GH concentrations applicable to any marine-geological environment.

However, although we were able to provide useful estimates of averaged values for FF at active and passive margins, fluid advection still remains a critical parameter, especially for active margins. For example, it is known from accretionary margins that fluid flow changes with the distance from the wedge (e.g. Breen and Orange, 1992; Saffer and Tobin, 2011), and hence may cause significant regional variations in the GH inventory. Consequently, any type of regional heterogeneity not resolved in the data base will introduce a fairly unknown degree of uncertainty, which clearly shows the need for improved fluid budgets along continental margins. Similarly, another critical issue is that all model runs were performed assuming steady-state conditions on time scales of several millions of years (Marquardt et al., 2010) assuming major control parameters (heat flow, POCar, FF) were constant. Hence, the model runs as well as the transfer functions do not consider any temporal variations of the sedimentary system. However, improved simulations in this regard are likely impossible as they by far exceed available data sources (at least on a global scale).

Overall, we believe that our study provides an improved and well constrained estimate for the global inventory of GH in marine sediments of 400–1100 GtC. Since the ascent of free methane gas, as another important, but completely unconstrained parameter could not be included one may still consider this value as a minimum estimate.

4 Conclusions

Our study shows that the global inventory of marine GH can be reliably estimated by the application of transfer functions that were derived from systematic runs of numerical transport-reaction model. Essentially, GH formation in marine sediments is determined by the thickness of the GHSZ, the POCar, and upward fluid advection. Without considering FF, hence, implying that continental margins are essentially diffusion-controlled

BGD
9, 581–626, 2012

sedimentary systems, would imply that only up to 91 GtC were stored in marine GH. Under these conditions GH would only form in areas of extremely high organic matter input, such as the margins of Angola-Namibia, India, and Peru, as well as in the Arabian Sea and the Arctic Ocean. The new transfer function developed in this study explicitly considering FF (0.10–0.20 and 0.02–0.03 mm yr^{-1} at active and passive margins, respectively) predicts minimum GH concentrations of 3–4 $gCH_4\,cm^{-2}$ for almost all continental margins worldwide, with significantly increased concentrations along the Japanese and Taiwanese margins, as well as in the American Pacific margin. The global inventory is estimated to be in the range of 400–1100 GtC. Our results suggest that the ascent of methane-rich fluids is a dominant process controlling GH formation and that this is not restricted to sites of focused fluid advection. Due to missing constraints on the upward migration of free methane gas into the GHSZ we still consider the values above as minimum estimates.

Acknowledgements. This work was conducted within the project SUGAR (Submarine Gas Hydrate Reservoirs) funded by the German Ministry of Education and Research (BMBF) and previously within the project HYDRA funded by the German Science Foundation (DFG). The authors would like to thank I. Grevemeyer and A. Biastoch for helpful advice and supply of data as well as M. Jegen and I. Segura for programming help.

References

Adam, D.: Methane Hydrates: Fire from ice, Nature, 418, 913–914, doi:10.1038/418913a, 2002.

Amante, C. and Eakins, B. W.: ETOPO1 1 Arc-Minute Global Relief Model: Procedures, Data Sources and Analysis, NOAA Technical Memorandum NESDIS NGDC-24, 19 pp., March 2009.

Archer, D.: Methane hydrate stability and anthropogenic climate change, Biogeosciences, 4, 521–544, doi:10.5194/bg-4-521-2007, 2007.

Archer, D., Buffet, B., and Brovkin, V.: Ocean methane hydrates as a slow

BGD
9, 581–626, 2012

tipping point in the global carbon cycle, P. Natl. Acad. Sci. USA, Special Feature, doi:10.1073/pnas.0800885105, 2009.
Barnier, B., Madec, G., Penduff, T., Molines, J.-M., Treguier, A.-M., Le Sommer, J., Beckmann, A., Biastoch, A. Böning, C., Dengg, J., Derval, C., Durand, E., Gulev, S., Remy, E., Talandier, C., Theetten, S., Maltrud, M., McClean J., and de Cuevas B.,: Impact of partial steps and momentum advection schemes in a global ocean circulation model at eddy-permitting resolution, Ocean Dynam., 56, 543–567, doi:10.1007/s10236-006-0082-1, 2006.
Baturin, G. N.: Issue of the relationship between primary productivity of organic carbon in ocean and phosphate accumulation (Holocene – Late Jurassic), Lithol. Miner. Resour., 42, 318–348, 2007.
Biastoch, A., Treude, T., Rüpke, L.H., Riesbesell, U., Roth, C., Burwicz, E.B., Park, W., Latif, M., Böning, C.W., Madec, G., and Wallmann, K.: Rising Arctic Ocean temperatures cause gas hydrate destabilization and ocean acidification, Geophys. Res. Lett., 38, L08602, doi:10.1029/2011GL047222, 2011.
Boswell, R.: Is gas hydrate energy within reach?, Science, 326, 957–958, doi:10.1126/science.1175074, 2009.
Breen, N. A. and Orange, D. L.: The effects of fluid escape on accretionary wedges I: variable porosity and wedge convexity, J. Geophys. Res., 97, 9265–9275, 1992.
Buffet, B. and Archer, D.: Global inventory of methane clathrate: sensivity to changes in the deep ocean, Earth Planet. Sci. Lett., 227, 185–199, doi:10.1016/j.epsl.2004.09.005, 2004.
Burdige, D. J.: Preservation of Organic Matter in Marine Sediments: Controls, Mechanisms, and an Imbalance in Sediment Organic Carbon Budgets?, Chem. Rev., 107, 467–485, doi:10.1021/cr050347q, 2007.
Burwicz, E., Rupke, L. H., and Wallmann, K.: Estimation of the global amount of submarine gas hydrates formed via microbial methane formation based on numerical reaction-transport modeling and a novel parameterization of Holocene sedimentation, Geochim. Cosmochim. Ac., 75, 4562–4576, doi:10.1016/j.gca.2011.05.029, 2011.
Cai, W.-J. and Reimers, C. E.: Benthic oxygen flux, bottom water oxygen concentration and core top organic carbon content in the deep northeast Pacific Ocean, Deep-Sea Res. I, 42, 1681–1699, 1995.
C. Clauser and Huenges, E.: Thermal conductivity of rocks and minerals, in: Rock Physics and Phase Relations – a Handbook of Physical Constants, edited by: Ahrens, T. J., AGU Reference Shelf, 3, 105–126, 1995.

BGD
9, 581–626, 2012

Collett, T. S.: Gas Hydrate Resources of the United States, in 1995 National Assessment of United States Oil and Gas Resources, on CD-ROM; edited by: Gautier, D. L., Dolton, G. L., Takahashi, K. I., and Varnes, K. L., USGS Digital Data Series, 30, pp. 85, 1995.

Davie, M. K. and Buffett, B. A.: A numerical model for the formation of gas hydrate below the seafloor, J. Geophys. Rev., 106, 497–514, doi:10.1029/2000JB900363, 2001.

Deming, D., Nunn, J. A., and Jones, S.: Some problems in thermal history studies, in: Applications of thermal maturity studies to energy exploration: Society of Economic Paleontologists and Mineralogists, edited by: Nuccio, V. F. and Barker, C. E., Rocky Mountain Section, 61–80, 1989.

Dickens, G. R.: The potential volume of oceanic methane hydrates with variable external conditions, Org. Geochem., 32, 1179–1193, doi:10.1016/S0146-6380(01)00086-9, 2001.

Divins, D. L.: NGDC Total Sediment Thickness of the World's Oceans and Marginal Seas, available at: http://www.ngdc.noaa.gov/mgg/sedthick/sedthick.html, 2 July 2010, 2010.

Dobrynin, V. M., Korotajev, Y. P., and Plyuschev, D. V.: Gas hydrates-one of the possible energy sources, in: Long-Term Energy Resources, edited by: Meyer, R. G. and Olson, J. C., 727–729, Pitman, Boston, MA, 1981.

Duan, Z. and Mao, S.: A thermodynamic model for calculating methane solubility, density and gas phase composition of methane-bearing aqueous fluids from 273 to 523 K and from 1 to 2000 bar, Geochim. Cosmochim. Ac., 70, 3369–3386, 2006.

Einsele, G.: Sedimentary Basins: Evolution, Facies and Sediment Budget, 2Ed.,792 pp., Springer, Berlin, 2000.

Fjeldskaar, W., Christie, O. H. J., Midttømme, K., Virnovsky, G., Jensen, N. B., Lohne, A., Eide, G. I., and Balling, N.: On the determination of thermal conductivity of sedimentary rocks and the significance for basin temperature history, Petrol. Geosci., 15, 367–380, doi:10.1144/1354-079309-814, 2009.

Floegel, S., Wallmann, K., Poulsen, C. J., Zhou, J., Oschiles, A., Voigt, S., and Kuhnt, W.: Simulating the biogeochemical effects of volcanic CO_2 degassing on the oxygen-state of the deep ocean during the Cenomanian/Turonian Anoxic Event (OAE2), Earth and Planet. Sci. Lett., 305, 371–384, doi:10.1016/j.epsl.2011.03.018, 2011.

Gornitz, V. and Fung, I.: Potential distribution of methane hydrates in the world's oceans, Global Biogeochem. Cy., 8, 335–347, 1994.

Grevemeyer, I., Kopf, A. J., Fekete, N., Kaul, N., Villinger, H. W., Heesemann, M., Wallmann, K., Spieß, V., Gennerich, H.-H., Müller, M., Weinrebe, W.: Fluid flow through active mud dome

BGD
9, 581–626, 2012

Mound Culebra offshore Nicoya Peninsula, Costa Rica: evidence from heat flow surveying, Mar. Geol., 207, 145–157, doi:10.1016/j.margeo.2004.04.002, 2004.
Hamza, V. M., Cardoso, R. R., and Ponte Neto, C. F.: Spherical harmonic analysis of the Earth's conductive heat flow, Int. J. Earth Sci. (Geol. Rundsch), 97, 205–226, doi:10.1007/s00531-007-0254-3, 2008.
Hartnett, H. E., Keil, R. G., Hedges, J. I., and Devol, A. H.: Influence of oxygen exposure time on organic carbon preservation in continental margin sediments, Nature, 391, 572–574, 1998.
Hartnett, H. E. and Devol, A. H.: Role of a strong oxygen-deficient zone in the preservation and degradation of organic matter: A carbon budget for the continental margin of northwest Mexico and Washington State, Geochim. Cosmochim. Ac., 67, 247–264, doi:10.1016/S0016-7037(02)01076-1, 2003.
Henrichs, S. M.: Early diagenesis of organic matter in marine sediments: progress and perplexity, Mar. Chem., 39, 119–149, 1992.
Hester, K. C. and Brewer, P. G.: Clathrate hydrates in Nature, Annu. Rev. Mar. Sci., 1, 303–327, doi:10.1146/annurev.marine.010908.163824, 2009.
Holbrook, W. S., Hoskins, H., Wood, W. T., Stephen R. A., and Lizarralde, S.: Methane Hydrate and Free Gas on the Blake Ridge form Vertical Seismic profiling, Science, 27, 1840–1843, doi:10.1126/Science.273.5283.1840, 1996.
Hustoft, S., Bunz, S., Mienert, J., and Chand S.: Gas hydrate reservoir and active methane-venting province in sediments on <20 Ma young oceanic crust in the Fram Strait, offshore NW-Svalbard, Earth Planet. Sc. Lett., 284, 12–24, doi:10.1016/j.epsl.2009.03.038, 2009.
Jarrard, R. D.: Subduction fluxes of water, carbon dioxide, chlorine, and potassium, Geochem. Geophys. Geosyst., 4, 8905, doi:10.1029/2002GC000392, 2003
Jung, W. Y. and Vogt, P. R.: Effects of bottom water warming and sea level rise on Holocene hydrate dissociation and mass wasting along the Norwegian-Barents Continental Margin, J. Geophys. Res., 109, B06104, doi:10.1029/2003JB002738, 2004.
Kaul, N., Foucher, J.-P., and Heesemann, M.: Estimating mud expulsion rates from temperature measurements on Hakon Mosby Mud Volcano, SW Barents Sea, Mar. Geol., 229, 1–14, doi:10.1016/j.margeo.2006.02.004, 2006.
Kastner, M.: Oceanic minerals: Their origin, nature of their environment, and significance, P. Natl. A. Sci. USA, 99, 3380–3387, doi:10.1073/pnas.96.7.3380, 1999.
Klauda, J. B. and Sandler, S. I.: Global Distribution of Methane Hydrate in Ocean Sediment,

BGD
9, 581–626, 2012

Energ. Fuel, 19, 459–470, doi:10.1021/ef049798o, 2005.
Kopf, A. J.: Significance of mud volcanism, Rev. Geophys., 40, 1005, doi:10.1029/2000RG000093, 2002.
Kvenvolden, K. A. and Claypool, G. E.: Gas hydrates in oceanic sediment, US Geological Survey Open-File Report, 88–216, 1988.
Kvenvolden, K. A. and Lorenson, T. D.: The global occurrence of natural gas hydrates, in: Natural Gas Hydrates: Occurrence, Distribution, and Detection, edited by: Paull, C. K. and Dillon, W. P., AGU, Washing, DC, 3–18, 2001.
Linke, P., Wallmann, K., Suess, E., Hensen, C., and Rehder, G.: In situ benthic fluxes from an intermittently active mud volcano at the Costa Rica convergent margin, Earth Planet. Sci. Lett. 235, 79–95, doi:10.1016/j.epsl.2005.03.009, 2005.
Lorenson, T. D. and Kvenvolden, K. A.: A Global Inventory of Natural Gas Hydrate Occurrence (Map), US Geological Survey, California, 2007.
Lunt, D. J., Ridgwell, A., Sluijs, A., Zachos, J., Hunter, S., and Haywood, A.: A model for orbital pacing of methane hydrate destabilization during the Palaeogene. Nat. Geosci., 4, 775–778, doi:10.1038/NGEO1266, 2011
MacDonald, G. J.: Global Climatic Change, in: Global Climate and Ecosystems Change edited by: MacDonald, G. J. and Sertorio, L., Plenum Press, New York, 247pp., 1990.
Makogon, Y. F.: Hydrates of Hydrocarbons, Penn Well Publishing Company, Tulsa, 504pp., 1997.
Malinverno, A., Kastner, M., Torres, M. E., and Wortmann, U. G.: Gas hydrate occurrence from pore water chlorinity and downhole logs in a transect across the northern Cascadia margin (Integrated Ocean Drilling Program Expedition 311), J. Geophys. Res., 113, B08103, doi:10.1029/2008JB005702, 2008.
Marquardt, M., Hensen, C., Piero, E., Wallmann, K., and Haeckel, M.: A transfer function for the prediction of gas hydrate inventories in marine sediments, Biogeosciences, 7, 2925–2941, doi:10.5194/bg-7-2925-2010, 2010.
Martens, C. S., Haddad, R. I., and Chanton, J. P.: Organic matter accumulation, remineralization, and burial in an anoxic coastal sediment, in: Organic matter: productivity, accumulation and preservation in recent and ancient sediments, edited by: Whelan, J. K. and Farrington, J. W., Columbia University Press, NY, 82–98, 1992.
Maslin, M. A., Owen, M., Betts, R., Day, S., Dunkley Jones, T., and Ridgwell, A.: Gas hydrates: Past and Future Geohazard?, Philos. T. R. Soc. A, 368, 2369–2393,

BGD
9, 581–626, 2012

doi:10.1098/rsta.2010.0065, 2010.
Mazurenko, L. L. and Soloviev, V. A.: Worldwide distribution of deep-water fluid venting and potential occurrences of gas hydrate accumulations, Geo.-Mar. Lett., 23, 162–176, doi:10.1007/s00367-003-0146-x, 2003.
Middelburg, J.: A simple rate model for organic matter decomposition in marine sediments, Geochim. Cosmochim. Ac., 53, 1577–1581, 1989.
Milkov, A. V.: Global estimates of hydrate-bound gas in marine sediments: how much is really out there?, Earth-Sci. Rev., 66, 183–197, doi:10.1016/j.earscirev.2003.11.002, 2004.
Milkov, A. V.: Molecular and stable isotope compositions of natural gas hydrates: A revised global dataset and basic interpretations in the context of geological settings, Org. Geochem., 36, 681–702, doi:10.1016/j.orggeochem.2005.01.010, 2005.
Milkov, A. V. and Sassen, R.: Economic geology of offshore gas hydrate accumulations and provinces, Mar. Petrol. Geol., 19, 1–11, doi:10.1016/S0264-8172(01)00047-2, 2002.
Moore, J. C. and Vrolijk, P.: Fluids in accretionary prisms, Rev. Geophys., 30, 113–135, 1992.
NOAA, Science on a Sphere: Age of the Sea Floor, available at: http://sos.noaa.gov/datasets/Land/sea_floor_age.html, 2 July 2010, 2010.
Pecher, I. A., Ranero, C. R., von Huene, R., Minshull, T. A., and Singh, S. C.: The nature and distribution of bottom simulating reflectors at the Costa Rican convergent margin, Geophys. J. Int., 133, 219–229, 1998.
Pollack, H. N., Hurter, S. J., and Johnson, J. R.: Heat flow from the Earth's interior: analysis of the global data set, Rev. Geophys., 31, 267–280, 1993.
Reitz, A., Haeckel, M., Wallmann, K., Hensen, C., and Heeschen, K.: Origin of salt-enriched pore fluids in the northern Gulf of Mexico, Earth Planet. Sci. Lett., 259, 266–282, doi:10.1016/j.epsl.2007.04.037, 2007.
Riedel, M., Willoughby, E. C., Chen, M. A., He, T., Novosel, I., Schwalenberg, K., Hyndman, R. D., Spence, G. D., Chapman, N. R., and Edwards, R. N.: Gas hydrate on the Northern Cascadia margin: regional geophysics and structural framework, in: Proc. IODP, 311, edited by: Riedel, M., Collett, T. S., Malone, M. J., and the Expedition 311 Scientists, Washington, DC (Integrated Ocean Drilling Program Management International, Inc.), doi:10.2204/iodp.proc.311.109.2006, 2006.
Romankevich, E. A., Vetrov, A. A., and Perespypkin, V. I.: Organic matter of the World Ocean, Rus. Geol. Geophys., 50, 299–307, doi:10.1016/j.rgg.2009.03.013, 2009.
Saffer, D. M. and Tobin, H. J.: Hydrogeology and mechanics of Subduction Zone Forearcs: Fluid

BGD
9, 581–626, 2012

flow and Pore Pressure, Annu. Rev. Earth Planet. Sci., 39, 157–86, doi:10.1146/annurev-earth-040610-133408, 2011.
Seiter, K., Hensen, C., Schröte, J., and Zabel, M.: Organic carbon content in surface sediments – defining regional provinces, Deep-Sea Res. I, 1–26, doi:10.1016/j.dsr.2004.06.014, 2004.
Seiter, K., Hensen, C., and Zabel, M.: Benthic carbon mineralization on a global scale, Global Biogeochem. Cy., 1–26, GB1010, doi:10.1029/2004GB002225, 2005.
Sloan, E. D.: Fundamental principles and applications of natural gas hydrates, Nature, 426, 353–363, doi:10.1038/nature02135, 2003.
Soloviev, V. A.: Global estimation of gas content in submarine gas hydrate accumulations, Russ. Geol. Geophysis., 43, 609–624, 2002.
Suess, E.: Particulate organic carbon flux in the oceans – surface productivity and oxygen utilization, Nature, 288, 260–263, 1980.
Tishchenko, P., Hensen, C., Wallmann, K., and Wong, C. S.: Calculation of the stability and solubility of methane hydrate in seawater, Chem. Geol., 219, 37–52, doi:10.1016/j.chemgeo.2005.02.008, 2005.
Torres, M. E., Wallmann, K., Tréhu, A. M., Bohrmann, G., Borowski, W. S., and Tomaru, H.: Gas hydrate dynamics at the Hydrate Ridge southern summit based on dissolved chloride data, Earth Planet. Sci. Lett., 226, 225–241, 2004.
Tromp, T. K., Van Cappellen, P, and Key, R. M.: A global model for the early diagenesis of organic carbon and organic phosphorous in marine sediments, Geochim. Cosmochim. A., 59, 1259–1284, 1995.
von Huene, R. and Scholl, D. W.: Observations at convergent margins concerning sediment subduction, subduction erosion, and the growth of continental crust, Rev. Geophys., 29, 279–316, 1991.
Wallmann, K., Linke, P., Suess, E., Bohrmann, G., Sahling, H., Chlüter, M., Dählmann, A., Lammers, S., Greinert, J., and Von Mirbach, N.: Quantifying fluid flow, solute mixing, and biogeochemical turnover at cold vents of the eastern Aleutian subduction zone, Geochem. Cosmochim. Ac., 61, 5209–5219, 1997.
Wallmann, K., Aloisi, G., Haeckel, M., Obzhirov, A., Pavlova, G., and Tishchenko, P.: Kinetics of organic matter degradation, microbial methane generation, and gas hydrate formation in anoxic marine sediments, Geochem. Cosmochim. Ac., 70, 3905–3927, doi:10.1016/j.gca.2006.06.003, 2006.
Wallmann, K., Burwicz, E., Ruepke, L., Marquardt, M., Pinero, E., Haeckel, M., and Hensen,

BGD
9, 581–626, 2012

C.: Constraining the global inventory of methane hydrate in marine sediments, Proceedings of the 7th International Conference on Gas Hydrates Edinburgh, 17–21 July, 2011.
Westrich, J. T. and Berner, R. A.: The role of sedimentary organic matter in bacterial sulfate reduction: The G model tested, Limnol. Oceanogr., 29, 236–249, 1984.
Wang, Y. and van Cappellen, P.: A multicomponent reactive transport model of early diagenesis: Application to redox cycling in coastal marine sediments, Geochim. Cosmochim. Ac., 60, 2993–3014, 1996.
Wood, W. T. and Jung, W.-Y.: Modeling the extent of Earth's marine methane hydrate cryosphere. Proceedings of the 6th International Conference on Gas Hydrates (ICGH 2008), Vancouver, British Columbia, Canada, 6–10 July, 2008.
Zonneveld, K. A. F., Versteegh, G. J. M., Kasten, S., Eglinton, T. I., Emeis, K.-C., Huguet, C., Koch, B. P., de Lange, G. J., de Leeuw, J. W., Middelburg, J. J., Mollenhauer, G., Prahl, F. G., Rethemeyer, J., and Wakeham, S. G.: Selective preservation of organic matter in marine environments; processes and impact on the sedimentary record, Biogeosciences, 7, 483–511, doi:10.5194/bg-7-483-2010, 2010.

BGD
9, 581–626, 2012

Table 1. Methane hydrate inventory calculated by several approaches and equations (see the text for details). GHI is the GH formed by methane generated through degradation of organic matter in the GHSZ, while GH_{FF} is the global result considering fluid advection. For the calculation of GH_{FF} (Eqs. 11a and b), 6 different combinations of fluid expulsion were applied at each scenario of POCar and heat flow, considering the global water expelled in margins ranging from 2 to 3.5 $km^3\,yr^{-1}$ (see text for details). The global integrated POCar for each scenario is also shown for comparison.

Scenario	Global	Global gas hydrate inventory [GtC]			
	POCar	Hamza's heat flow		Pollack's heat flow	
	[$gC\,yr^{-1}$]	GHI	GH_{FF}	GHI	GH_{FF}
1	1.44E + 14	1	451–832	1	372–669
2	1.54E + 14	91	674–1166	81	564–927
3	2.10E + 13	18	298–539	16	258–452
4	2.30E + 13	9	497–571	8	286–512

BGD
9, 581–626, 2012

Table 2. Input parameters and upper and lower boundary conditions for the standard model.

Parameter [unit]:	
Density of dry solids – d_s [g m^{-3}]	2.5
Porosity – ϕ $\phi = \phi_f + (\phi_0\text{-}\phi_f)\cdot e^{-px\cdot x}$	
ϕ_0, ϕ_f, px	0.75, 0.59, 0.02
Initial age of POC – age$_{init}$ [kyr]	43.7
NH_4 adsorption coefficient – K_{ads} [cm^3 g^{-1}]	0.52
POC inhibition constant – K_c [mmol l^{-1}]	43.7
Thickness of the GHSZ – L_{GHSZ} [m]	(228–1745)
POCar [g m^{-2} yr−1]	(0.7–37.4)
Fluid flow velocity – FF [mm yr^{-1}]	(0.05–2)
Upper boundary conditions:	
SO_4 concentration [mmol l^{-1}]	28
CH_4 concentration [mmol l^{-1}]	0
NH_4 concentration [mmol l^{-1}]	0
Lower boundary conditions:	
SO_4 concentration [mmol l^{-1}]	0
CH_4 concentration [mmol l^{-1}]	(55.5–204.8)
DIC concentration [mmol l^{-1}]	(104.4–328.5)
NH_4 concentration [mmol l^{-1}]	(12–38.2)

BGD
9, 581–626, 2012

Table 3. Global gas hydrate estimations (GH_{FF}) in GtC, calculated after Eqs. (11a) and (11b), for a number of combinations of the total volume of water expelled in the active and passive margins, applying a global volume of water expelled of 2–3.5 $km^3\,yr^{-1}$, scenario 2 for POCar, and Hamza's approach to calculate the heat flow. At active margins, a volume of 1 $km^3\,yr^{-1}$ of expelled water corresponds to a fluid velocity of 0.1027 $mm\,yr^{-1}$, 1.5 $km^3\,yr^{-1}$ to 0.1533 $mm\,yr^{-1}$, and 2 $km^3\,yr^{-1}$ to 0.2053 $mm\,yr^{-1}$. At passive margins, a volume of 1 $km^3\,yr^{-1}$ of expelled water corresponds to 0.02 $mm\,yr^{-1}$, and 1.5 $km^3\,yr^{-1}$ to 0.03 $mm\,yr^{-1}$.

Passive \ Active	1 $km^3\,yr^{-1}$	1.5 $km^3\,yr^{-1}$	2 $km^3\,yr^{-1}$
1 $km^3\,yr^{-1}$	674	878	1089
1.5 $km^3\,yr^{-1}$	751	955	1166

BGD
9, 581–626, 2012

Table A1. Linear correlation matrix for fit parameters of Eq. (1).

	a_1	a_2	a_3	a_4
a_1	1	−0.999	0.091	0.082
a_2	−0.999	1	−0.065	−0.062
a_3	0.091	−0.065	1	0.941
a_4	0.082	−0.062	0.941	1

BGD
9, 581–626, 2012

Table A2. Linear correlation matrix for fit parameters of Eq. (11).

	b_1	b_2	b_3	b_4	b_5	b_6	b_7	b_8	b_9
b_1	1	−0.176	0.248	−0.001	0.002	−0.723	−0.186	0.321	−0.511
b_2	−0.176	1	−0.709	0.047	0.052	0.104	0.690	−0.234	0.212
b_3	0.248	−0.709	1	−0.004	0.008	−0.181	−0.974	0.330	−0.300
b_4	−0.001	0.047	−0.004	1	−0.965	0.373	0.004	−0.001	0.001
b_5	0.002	0.052	0.008	−0.965	1	−0.421	−0.008	0.003	−0.002
b_6	−0.723	0.104	−0.181	0.373	−0.421	1	0.136	−0.233	0.370
b_7	−0.186	0.690	−0.974	0.004	−0.008	0.136	1	−0.117	0.115
b_8	0.321	−0.234	0.330	−0.001	0.003	−0.233	−0.117	1	−0.931
b_9	−0.511	0.212	−0.300	0.001	−0.002	0.370	0.115	−0.931	1

BGD
9, 581–626, 2012

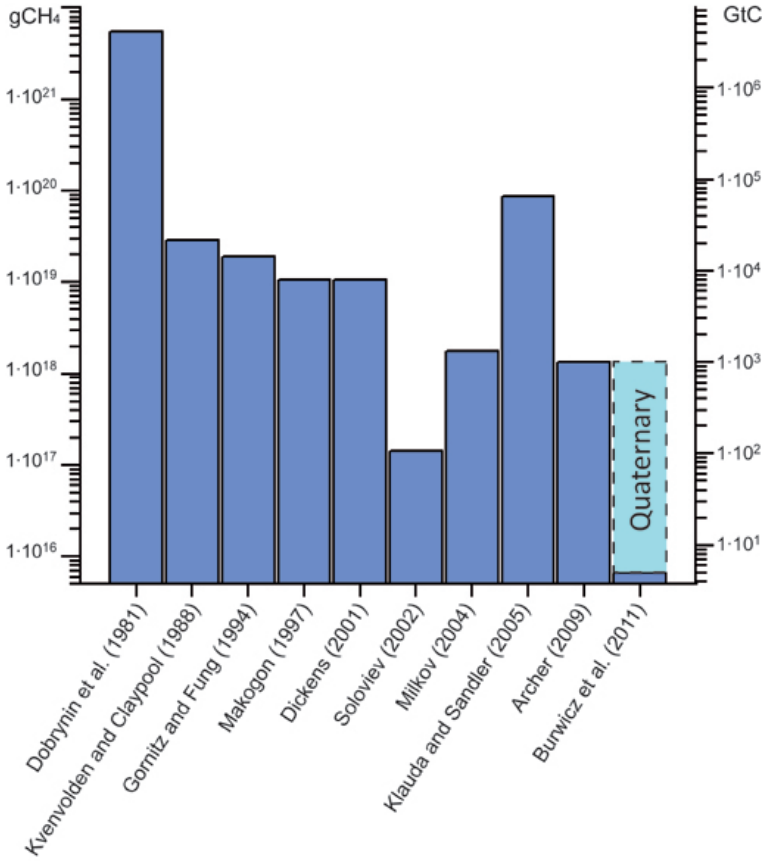

Fig. 1. Estimates of global gas hydrate inventories in marine sediments.

BGD
9, 581–626, 2012

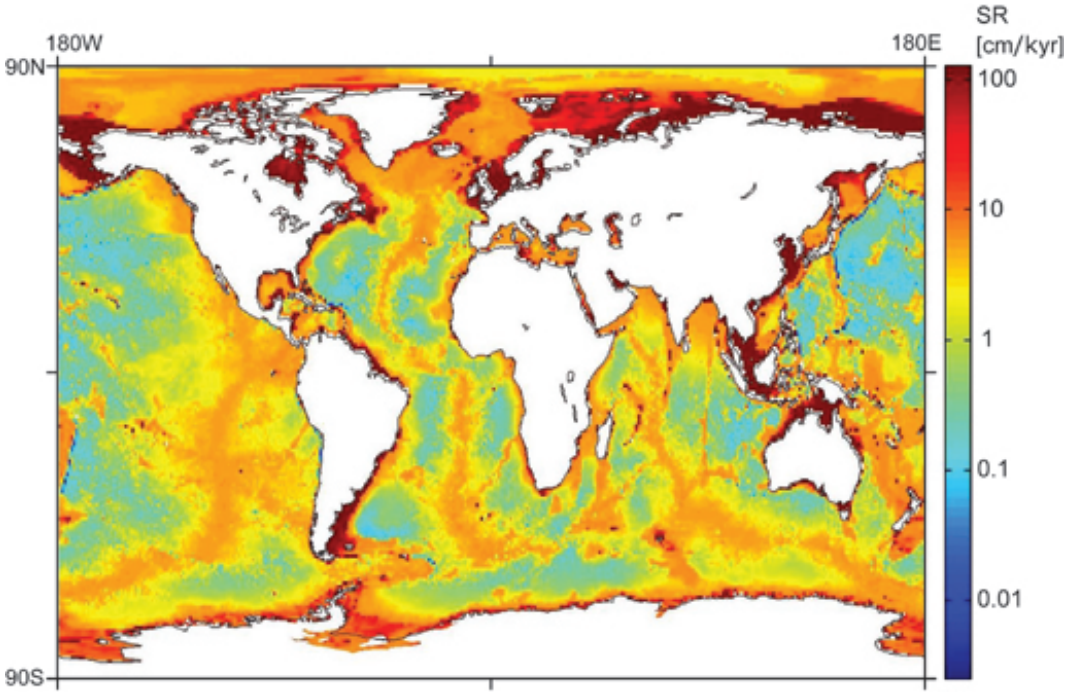

Fig. 2. Distribution map of the sedimentation rate (SR) calculated following Eq. (2). Note the logarithmic scale bar.

BGD
9, 581–626, 2012

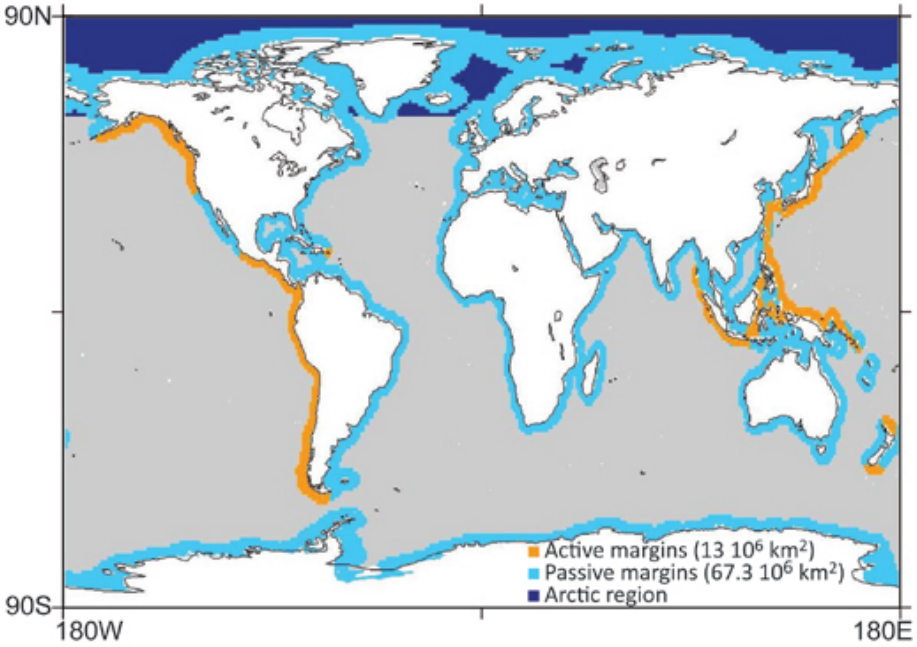

Fig. 3. Global map indicating margins and deep sea areas. The distinction between active (orange) and passive (light blue) margins is based on Archer et al. (2009). The total areas for active and passive margins calculated in a 1 × 1° basis are shown for comparison.

BGD
9, 581–626, 2012

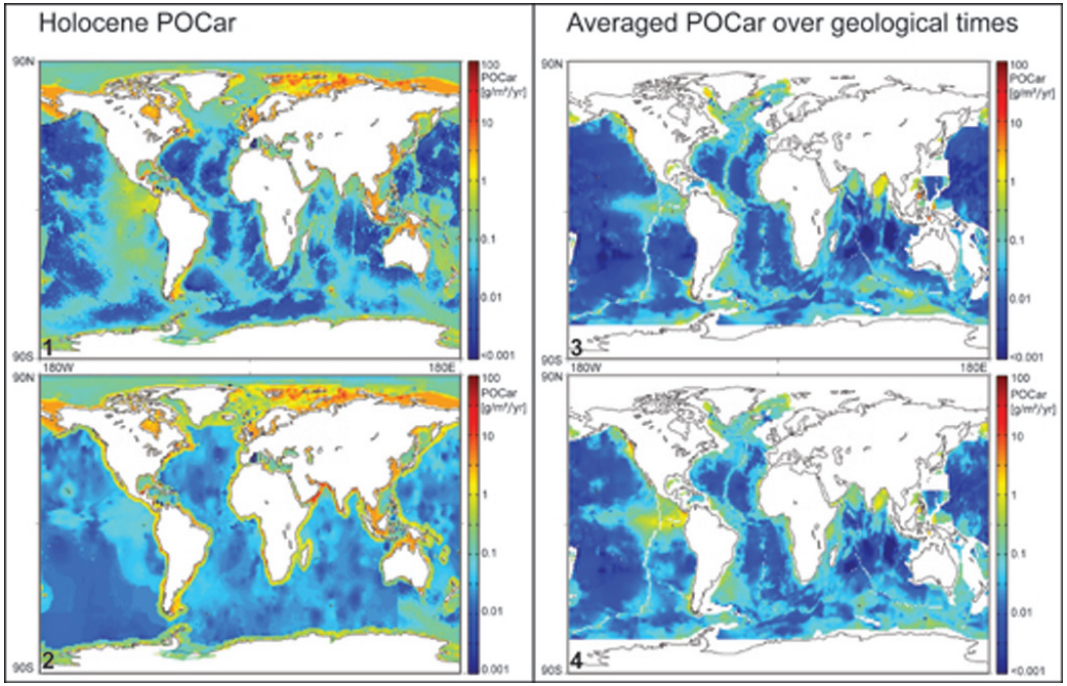

Fig. 4. Distribution map of the accumulation rate of particulate organic carbon, based on the four approaches (#1 to #4) presented in this work (see text for details). Note the logarithmic colour scales.

BGD
9, 581–626, 2012

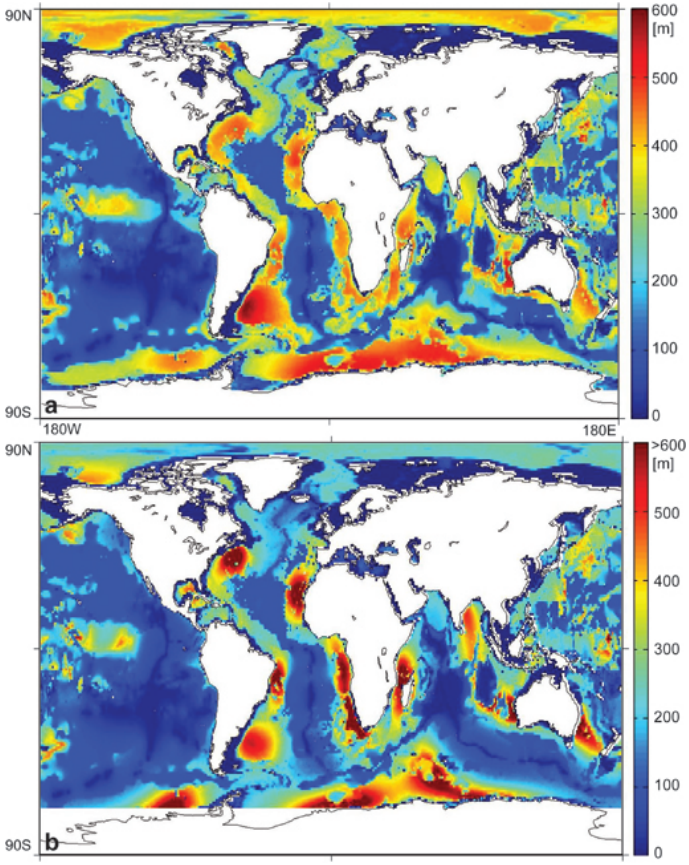

Fig. 5. Global distribution of the thickness of the gas hydrate stability zone (L_{GHSZ}); **(a)**. Geothermal gradient was calculated after the harmonic function of Hamza et al. (2008) to calculate heat flow and considering a thermal conductivity of 1 W K^{-1} m^{-1}; **(b)**. Geothermal gradient was calculated after the harmonic function published by Pollack et al. (1993) and considering a thermal conductivity of 1 W K^{-1} m^{-1}.

BGD
9, 581–626, 2012

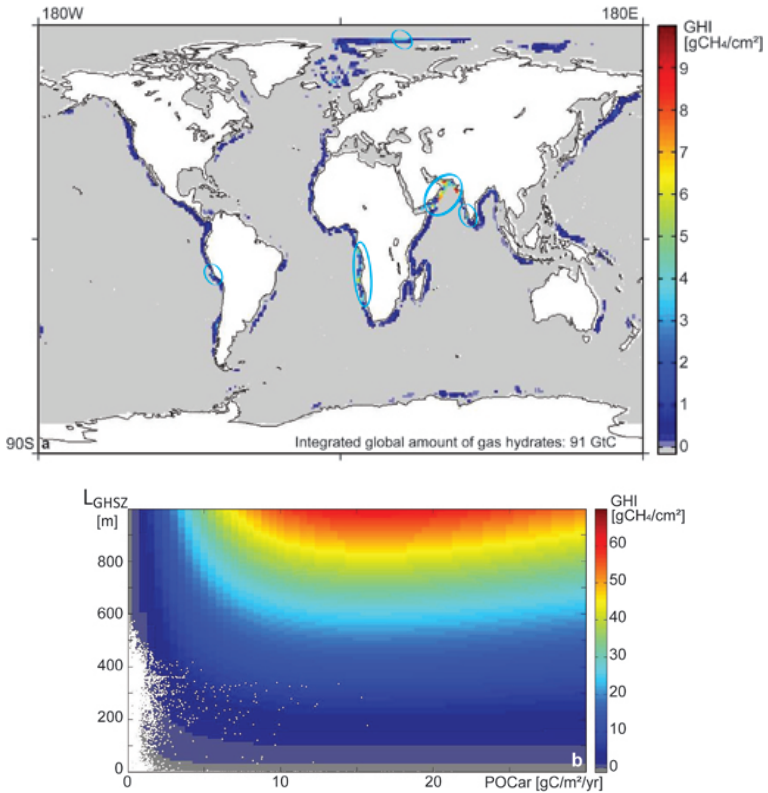

Fig. 6. Distribution map of the gas hydrates formed by methane generated through degradation of organic matter within the GHSZ (GHI, Eq. 1), considering Approach #2 for POCar and Hamza's dataset to calculate the thickness of the gas hydrate stability zone (L_{GHSZ}). Blue circles highlight the hydrate-rich areas. **(b)** Gas hydrate concentration predicted by the transfer function (Eq. 1) for a wide range of values of L_{GHSZ} and POCar. For comparison, the results obtained for the global distribution presented in **(a)** are plotted as white dots.

BGD
9, 581–626, 2012

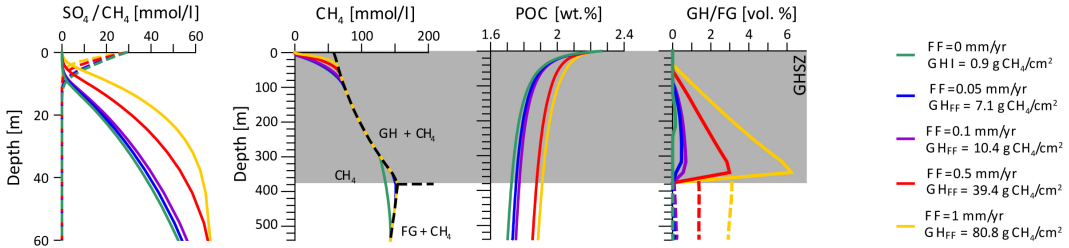

Fig. 7. Model results considering five different fluid advection rates (0, 0.05, 0.1, 0.5, and 1 mm yr^{-1}), for POCar of 4.34 gC m^{-2} yr^{-1} and L_{GHSZ} of 376 m, including concentration of dissolved sulfate (SO_4, dashed line), dissolved methane (CH_4), particulate organic carbon (POC), and concentrations of gas hydrates (GH) and free gas (FG; dashed line) below the gas hydrate stability zone (GHSZ). For these model runs concentrations at the lower boundary of CH_4, DIC and NH_4 were fixed respectively at 143.4, 247.6 and 25.6 mmol l^{-1}. Dissolution of methane hydrates (black dashed line in the CH_4 plot) was calculated using Tishchenko et al. (2005). Solubility of free methane gas (FG) was calculated after Duan and Mao (2006). Depth integrated masses of gas hydrates per area seafloor are provided (GHI or GH_{FF} in gCH_4 cm^{-2}).

BGD
9, 581–626, 2012

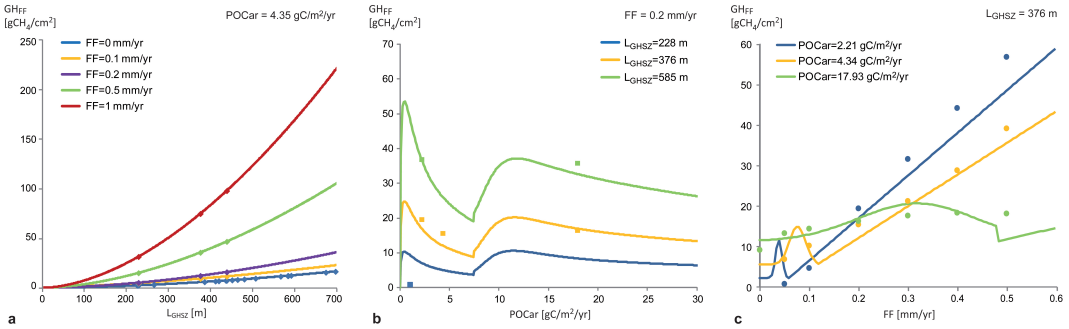

Fig. 8. Parameter analysis of the three control parameters POCar, thickness of the gas hydrate stability zone (L_{GHSZ}) and fluid flow (FF) for gas hydrate formation. The plots show the results of the model-runs as dots, and the results of Eqs. (11a) and (11b) as lines; **(a)**. Relation of L_{GHSZ} and gas hydrate accumulation (GH_{FF}) for varying FF, with constant POCar of 4.35 gC m^{-2} yr^{-1}; **(b)**. Relation of POCar and GH_{FF} for varying thickness of the GHSZ, with constant FF (0.2 mm yr^{-1}); and **(c)**. Relation of fluid flow and GH_{FF} for varying POCar, with a constant L_{GHSZ} (376 m).

BGD
9, 581–626, 2012

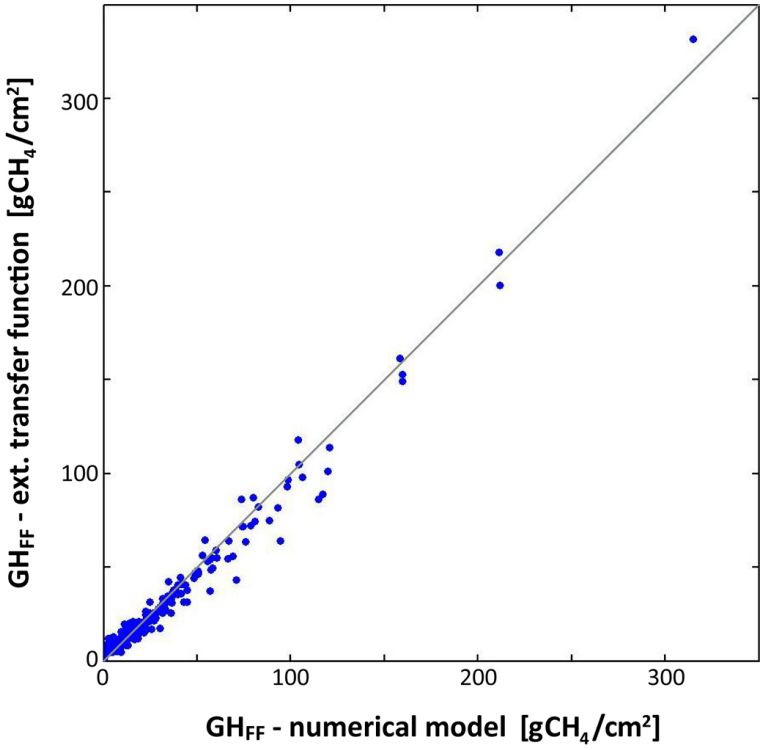

Fig. 9. Cross-plot of the depth integrated gas hydrate masses (GH_{FF}) estimated by the extended transfer function calculated following Eqs. (11a) and (11b) and by the numerical models. The solid line shows the 1:1 correlation.

BGD
9, 581–626, 2012

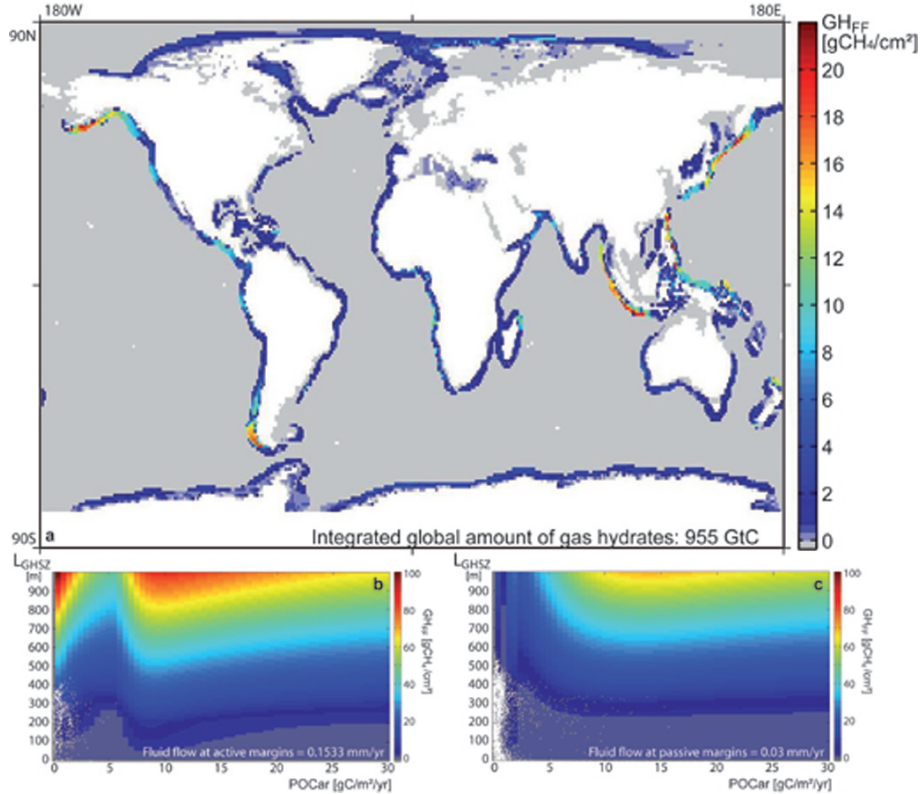

Fig. 10. Distribution map of the total methane hydrate budget considering fluid flow (GH_{FF}), calculated following Eqs. (11a) and (11b); **(b)**. Gas hydrate accumulation predicted by Eqs. (11a) and (11b) for a wide range of values of POCar and L_{GHSZ} in active continental margins. For comparison to real conditions, the results obtained for the global distribution map are plotted as white dots; **(c)**. Gas hydrates accumulation predicted by Eqs. (11a) and (11b) for a wide range of values of POCar and L_{GHSZ} in passive continental margins. The results obtained for the global distribution map are plotted as white dots.

BGD
9, 581–626, 2012

Estimation of the global inventory of methane hydrates

E. Piñero et al.

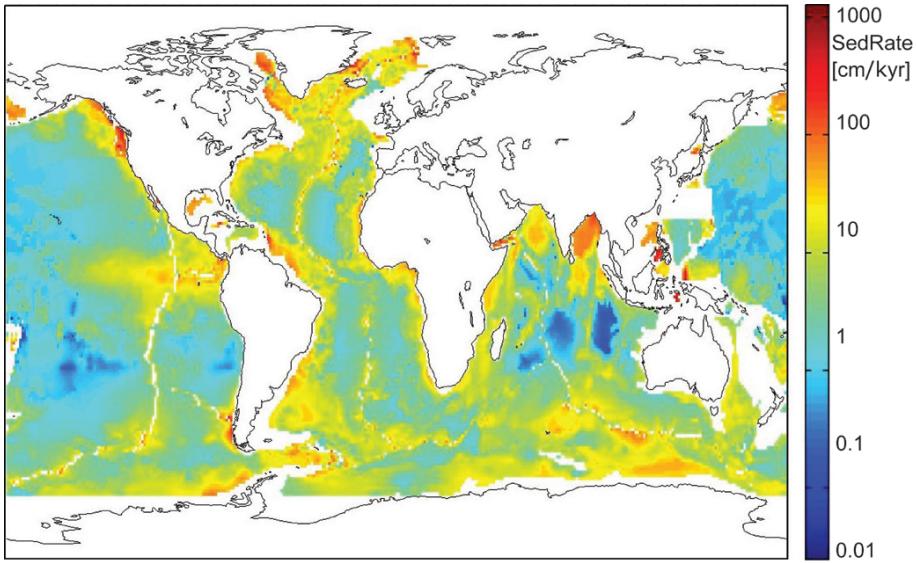

Fig. A1. Map of the averaged sedimentation rate over geological time scales calculated with global datasets of the total thickness of the sediment column and the age of the oceanic crust, following Eq. (7).

BGD
9, 581–626, 2012